

# **Measurement Uncertainties in X-ray Computed Tomography**

Joshua Greenhalgh

September 16, 2015



---

## ABSTRACT

---

X-ray computed tomography (XCT) is beginning to find a range of new industrial applications. For many years this technique has been applied to non-destructive testing (NDT), however it is now being used by industry for the purpose of metrology. XCT has certain advantages over the traditional approach to metrology that of the co-ordinate measuring machine (CMM). Foremost among these is the ability to measure both external and internal aspects of an object's geometry without the need to destroy the object. This technique does however suffer from the lack of a clear understanding of the processes metrological uncertainties - if XCT is to be adopted more widely then it is necessary to be able to quantify the underlying uncertainties in this measuring procedure. This Thesis will approach the problem of quantifying these uncertainties via the simulation of an XCT system. The focus will be on the effect of magnification on measurement uncertainty in the presence of realistically modelled source and detector elements.



---

## CONTENTS

---

1	INTRODUCTION	11
2	LITRATURE REVIEW	13
2.1	Metrology	13
2.2	Computed Tomography	13
2.3	Simulation	13
3	EXPERIMENTAL METHODOLGY	15
3.1	Intoduction	15
3.2	Spherical Projections and Reconstruction	15
3.3	Measurement	17
3.4	Calculation of the Modulation Transfer Function	18
3.4.1	Polar Method	19
3.5	Beam Hardening	19
4	RESULTS	21
4.1	Introduction	21
4.2	Measurement Uncertainty	21
4.3	Polychromatic Projections	26
4.4	Image Resolution - MTF half width	26
4.5	Analytic MTF	31
5	CONCLUSION	33



---

## LIST OF FIGURES

---

Figure 1	A digram showing a birds eye view of the XCT system	16
Figure 2	A 3D view of the XCT system showing the detector array	17
Figure 3	Showing the average radius at each magnification.	22
Figure 4	Showing the relative error of the radius measurement at each magnification.	22
Figure 5	Showing the variation of the radius measurement at each magnification.	23
Figure 6	Showing the variation of the radius measurement at each magnification.	24
Figure 7	Showing the variation of the radius measurement with a sample of 30 at each magnification.	25
Figure 8	Showing the measured position of the spheres centre	26
Figure 9	Showing the standard deviation of the measured position of the spheres centre	27
Figure 10	Showing the standard deviation of the measured position of the spheres centre	28
Figure 11	Showing the standard deviation of the measured position of the spheres centre	29
Figure 12	Showing the standard deviation of the measured position of the spheres centre	30
Figure 13	Showing the standard deviation of the measured position of the spheres centre	30
Figure 14	Showing the standard deviation of the measured position of the spheres centre	31
Figure 15	Showing the standard deviation of the measured position of the spheres centre	32





---

LIST OF TABLES

---

Table 1	Blah	11
Table 2		30
Table 3		31
Table 4		32



---

INTRODUCTION

---

Table 1: Blah

Magnification	SoDo	S1Do	SoD1	S1D1
1.5000	29.9141	29.8956	29.8804	29.8763
1.7778	29.8963	29.8871	29.8834	29.8776
2.0556	29.9046	29.8858	29.8867	29.8785
2.3333	29.9105	29.8859	29.8913	29.8796
2.6111	29.9020	29.8845	29.8929	29.8795
2.8889	29.8946	29.8828	29.8927	29.8788
3.1667	29.9036	29.8814	29.8940	29.8782
3.4444	29.9057	29.8805	29.8957	29.8776
3.7222	29.9034	29.8794	29.8957	29.8771
4.0000	29.9000	29.8781	29.8955	29.8760



---

## LITRATURE REVIEW

---

### 2.1 METROLOGY

### 2.2 COMPUTED TOMOGRAPHY

### 2.3 SIMULATION



---

## EXPERIMENTAL METHODOLOGY

---

### 3.1 INTRODUCTION

Section in which I outline what will follow in this chapter, also link to previous chapter!

### 3.2 SPHERICAL PROJECTIONS AND RECONSTRUCTION

The simulation of an X-ray computed tomography (XCT) system was undertaken using a previously developed set of Matlab routines (ref to avon). These routines consisted of functions that created projections of an analytically defined sphere and also produced a reconstructed volume via the FDK method (ref to feildkamp and literature). The simulation of a single projection, under the assumption of a point source and point like detector elements, consists of the following general process;

1. For the  $i^{th}$  element in the detector array form the ray which connects the source at position  $(s_x, s_y, s_z)^T$  with the detector element at position  $(d_x^i, d_y^i, d_z^i)^T$ .
2. Calculate the intersection of this ray with the sphere defined by  $\|x - c\| = r^2$  where  $c = (c_x, c_y, c_z)^T$  is the spheres centre and  $r$  is its radius.
3. For each ray that passes through the sphere calculate the distance between its entry and exit points.
4. Associate each path length with the correct detector element and form an array of path lengths.

Projections are calculated at a range of angles, for each angle the source and detector elements are rotated around the sphere. The detectors are arranged in a rectangular array such that both the source and detector elements lie in parallel planes. The distances from the source to the axis of rotation ( $D_{s \rightarrow r}$ ) and from the axis of rotation to the detector ( $D_{r \rightarrow d}$ ) are of particular importance - the ratio  $\frac{D_{s \rightarrow r} + D_{r \rightarrow d}}{D_{s \rightarrow r}}$  determines the magnification of the system. This means that an object of length  $x$  constrained to be on the plane parallel to the detector

and containing the axis of rotation will appear to have a length of  $\frac{x(D_{s \rightarrow r} + D_{r \rightarrow d})}{D_{s \rightarrow r}}$  on the detector. Intuitively magnification can be thought of as being high when the source is close to the object and low when it is far away - assuming a fixed distance from the source to the detector. A birds eye view of the XCT system is shown in figure 1 and a view of the detector elements (for a  $4 \times 4$  array) is shown in figure 2.

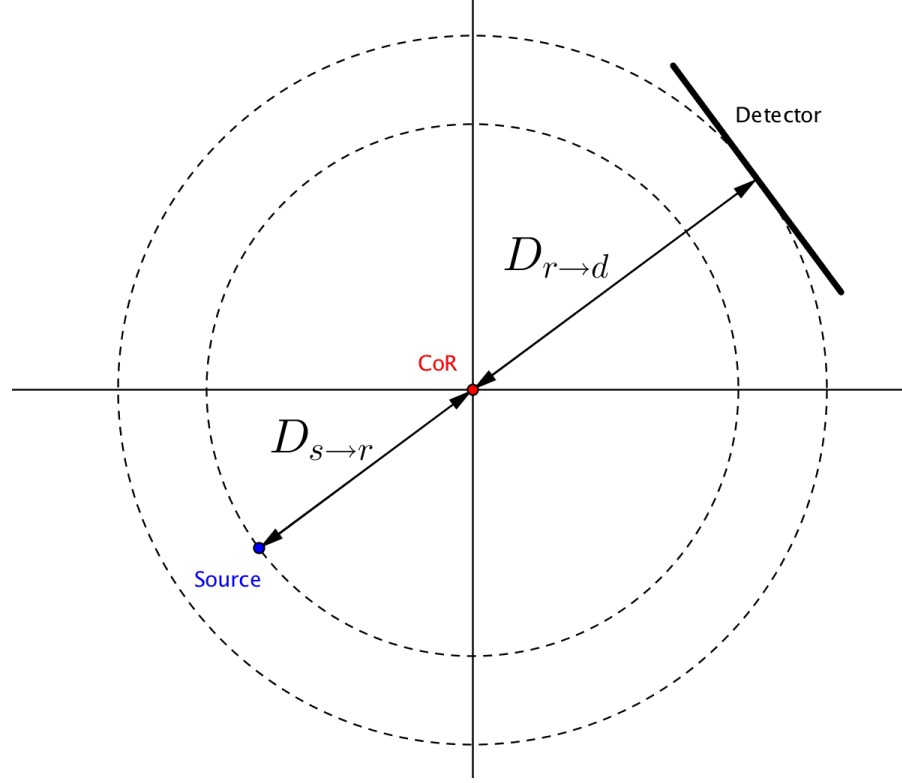


Figure 1: A digram showing a birds eye view of the XCT system

In order to simulate more realistic source and detector behavior the projection process is repeated many times at each angle with random offsets applied to the positions of the source and each detector element, the resulting projection values being the mean of the repetitions. In the case of the detector elements this entails adding an independent random offset to each detector element - not the same offset to all.

The experiments undertaken for this project involved the simulation of projections at 1000 angles between 0 and  $2\pi$ . The choice of this particular number of projections was chosen so as maximize the accuracy of the reconstructed volume whilst minimizing computational expense - an investigation of the effect of the number of projections used was not undertaken. The object imaged was a sphere of radius  $30mm$  with centre at  $c = (0,0,0)^T$ . An array of  $301 \times 301$  detector elements was used extending over an area of  $400mm \times 400mm$ . Four experimental treatments were investigated;



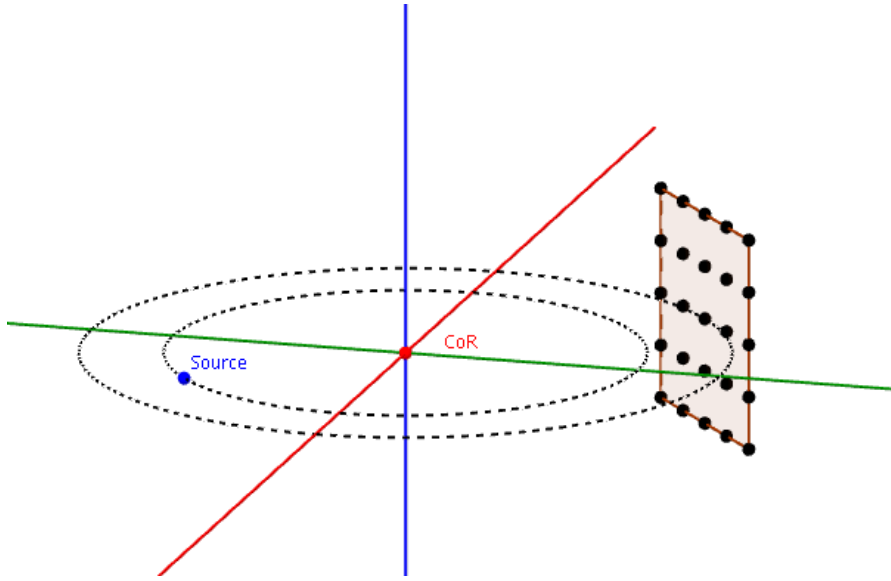


Figure 2: A 3D view of the XCT system showing the detector array

1. S0D0 - Ideal point like source and detector elements.
2. S1D0 - Random position offset applied to source (each component of the offset drawn from standard normal distribution), point like detector elements.
3. S0D1 - Random position offset applied independently to each detector element (each component of the offset drawn from standard normal distribution), point like source.
4. S1D1 - Random position offsets applied to both the source and the detector elements (each offset drawn from same distributions as above).

For each treatment projections were simulated at each of 10 equally spaced magnifications between 1.5 and 4.0. At a particular magnification 10 sets of projections were simulated. This leads to a total of 400 projections and reconstructions - consisting of four treatments, ten magnifications and ten repetitions at each magnification.

The resulting reconstructions consisted of a  $301 \times 301 \times 301$  array of voxels that extended from  $-35\text{mm}$  to  $35\text{mm}$  in all three coordinate directions.

### 3.3 MEASUREMENT

From a reconstructed volume it was necessary to obtain a series of measurements relating to the sphere. This was achieved by the extraction of surface points via a thresholding operation and edge detection and then the fitting of an analytical sphere to the surface data. The

Matlab function `post_proc_fixed_thresh.m` is used to achieve these operations. Thresholding was undertaken by simply defining all voxels greater than a value of 0.5 to be on the interior of the sphere and those smaller to be on the exterior. This resulted in a 3D array consisting of ones (for interior points) and zeros (for exterior points). By applying Matlab's inbuilt edge detection function to this array it was possible to arrive at a new array such that the voxels took a value of one on the surface of the sphere and a zero everywhere else. Using the surface data a sphere was fitted using a least squares method which resulted in the parameters of a sphere in terms of the array indices. In order to convert from array indices to actual physical coordinates it was necessary, in the case of the spheres radius, to multiply the values by the voxel size ( $\Delta v = \frac{70}{301}$ ) and also for the position of the centre to offset by subtracting  $35mm$ . So given a fitted sphere with the following parameters;

$$r = 128$$

$$C_x = C_y = C_z = 150$$

The parameters given in physical coordinates would be given by;

$$r = 128\Delta v$$

$$C_x = C_y = C_z = -35 + 150\Delta v$$

The value of the radius gained from this procedure along with the position of the spheres centre were used in order to analyse the XCT system's uncertainty. Along with the above described method for determining the spheres radius another method was implemented in order to validate the results - this method will be described in the next section.

### 3.4 CALCULATION OF THE MODULATION TRANSFER FUNCTION

The calculation of the Modulation Transfer Function (MTF) was undertaken via two separate methods. The methods differ in how edge profiles were extracted from the reconstructed volume. The first method used all the voxels in a plane via a polar reparameterisation of the voxel coordinates whilst the second method involved the 3D interpolation of the volume along rays emanating from the spheres centre.

The need for interpolation arises since the change from interior to exterior of the sphere takes place over around 2 voxels. This means that there is not enough information to accurately calculate the MTF. It was also desirable to calculate the MTF in directions other than the coordinate axis.

## 3.4.1 Polar Method

The first method implemented is described in refA simple approach.... From the voxel array it is possible to extract three slices (xy-plane,xz-plane and the yz-plane). The voxels in each slice can be given coordinates in the following way;

$$\begin{aligned} V_{i,j} &\rightarrow (-35 + \Delta xi, -35 + \Delta yj) \\ i, j &= 0, \dots, 300 \\ \Delta x &= \frac{70}{300} = \Delta y \end{aligned}$$

In order to form an edge profile from the slice we convert from cartesian coordinates to polar, only taking account of the radial distance from the origin. A given voxel with cartesian coordinates  $(x, y)$  has radial distance  $r = x^2 + y^2$ . By sorting the voxels by radial distance are able to obtain an edge profile, however this profile is multi-valued in that there exist multiple voxels with the same radial distance. To produce a one-to-one mapping between radial distance and voxel intensity we associate to a particular radial distance the average of all voxels at this distance. The resulting profile is however rather noisy and as such is not suitable for calculating the MTF - in order to rectify this situation the method in refsigmoid ref has been used. This method takes the noisy edge profile and fits a sigmoid function of the following form;

$$S(x) = \frac{a}{1 + e^{-b(x-c)}} + d$$

The sigmoid function is chosen since it takes the approximate form of a step function for certain values of the parameters. An example of this function is shown in figsigmoid. Once the parameters of the fitted function are known it is possible to sample the edge at 100 points between 25mm and 35mm giving a sample rate of 10 samples/mm. The sampled edge profile is then numerically differentiated and by taking the absolute value of the FFT we arrive at the MTF of the system. As a by product of this technique for calculating the MTF it is also possible to arrive at an independent estimate of the spheres radius. The parameter  $d$  in the sigmoid function determines the point at which the function behaves like a step and this can be used to estimate the distance at which the transition from interior to exterior of the sphere occurs. This particular technique for measuring the radius is only possible due to the symmetrical nature of the object being imaged.

## 3.5 BEAM HARDENING



---

## RESULTS

---

### 4.1 INTRODUCTION

Section in which I outline what will follow in this chapter, also link to previous chapter!

### 4.2 MEASUREMENT UNCERTAINTY

Initially we will look at the average radius, taken over ten repetitions, at each level of magnification. In figure 3 we can see the plot of this measurement for each of the four experimental treatments; ideal source and detector (*S0D0*), non-ideal source and ideal detector (*S1D0*), ideal source and non-ideal detector (*S0D1*) and non-ideal source and detector (*S1D1*). As can be seen from the plot all measurements are systematically biased below the true value of the imaged object (30mm). There exist clear trends in the behavior of the measurement as magnification increases for *S1D0*, *S0D1*, and *S1D1*. The ideal imaging system (*S0D0*) exhibits a less clear trend, seeming to be highly noisy.

We can also look at the relative error of the measurements since we are in the position of knowing the true value - this can be seen in figure 4. The *S0D0* treatment shows the lowest relative errors of all treatments, there appears to be an increase in the error as magnification increases however the data is rather noisy. Treatments *S1D0* and *S0D1* show opposing, possibly linear, trends. Measurements taken with a non-ideal detector seem to get more accurate as magnification increases whereas the measurements taken with a non-ideal source show a decrease in the accuracy with an increase in magnification. When the measurements are taken with both non-ideal source and detector the relative errors are the largest of all treatments. There appears to be a non-linear, perhaps quadratic, relation between magnification and measurement error.

It should be noted that all the measured errors are at the sub-voxel level; the largest error seen is around 0.4% which equates to an actual deviation from the true value of around 0.12mm less than 2% of the voxel width (4.2mm).

## RESULTS

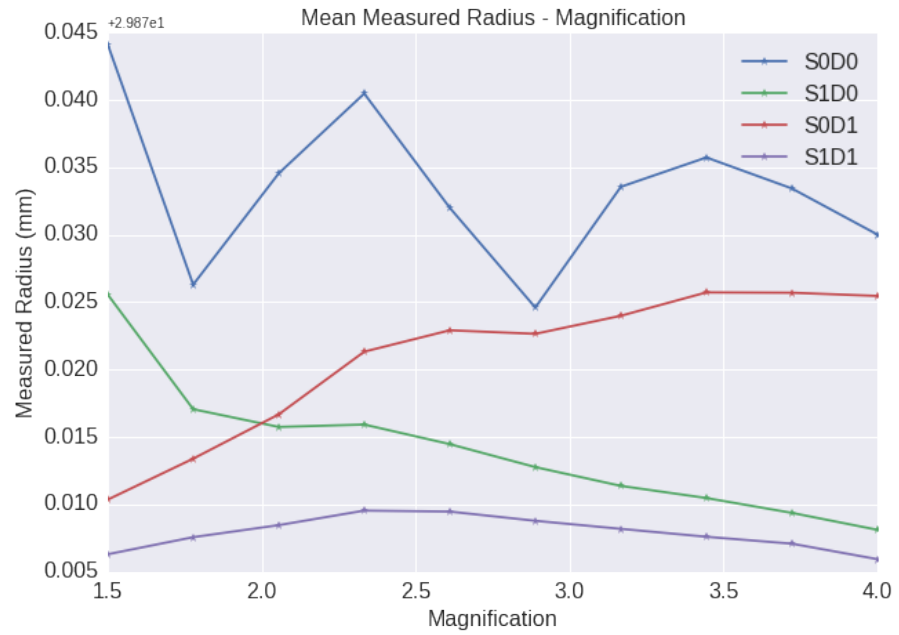


Figure 3: Showing the average radius at each magnification.

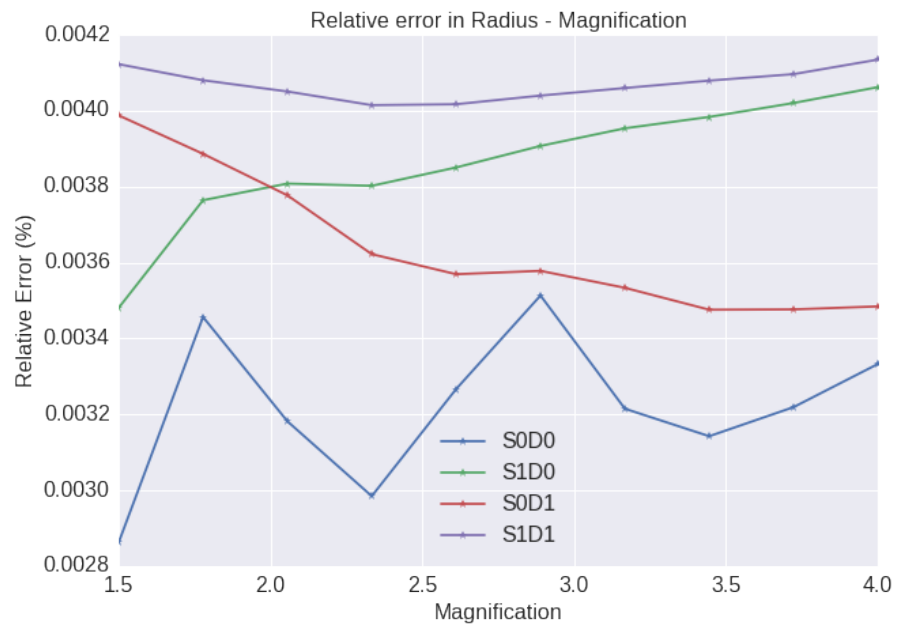


Figure 4: Showing the relative error of the radius measurement at each magnification.

As an independent check on the trends observed it was also possible to calculate an estimate of the radius from the parameters of the function fitted to calculate the MTF. In figure 5 we see the relative error of the measurements gained via this method. As can be seen in the figure the general trends are replicated via this secondary method however the actual errors are an order of magnitude smaller.

The use of this method for calculating the radius when applied to the S0D0 treatment resulted in very different measurements and so is not shown in the figure. (WHY IN CONCLUSIONS)

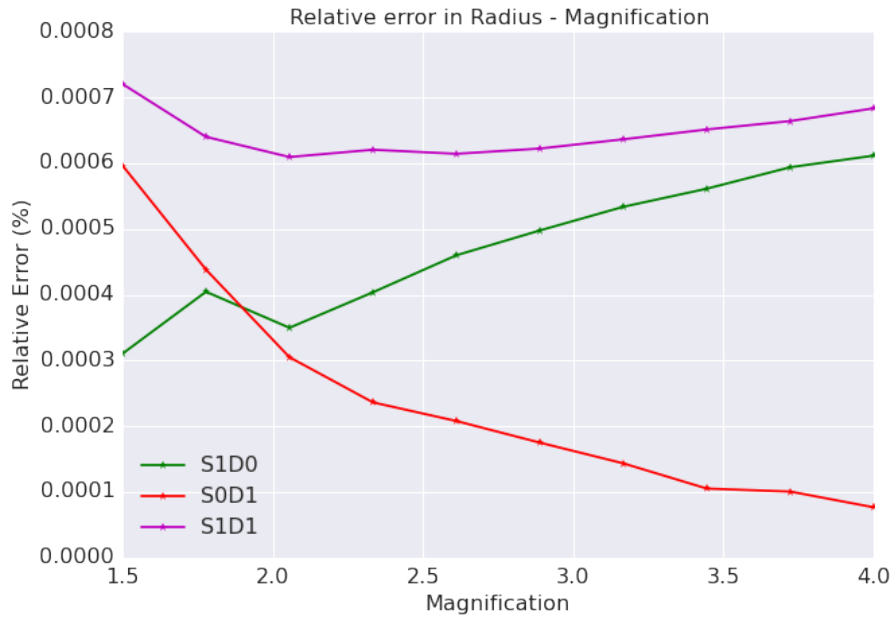


Figure 5: Showing the variation of the radius measurement at each magnification.

In figure 6 we can see the variation (standard deviation) in the measurement in relation to magnification. This data is only available for S1D0, S0D1 and S1D1. This is because with an ideal source and detector the measurement is in effect deterministic. The projections do have very small additive noise applied but this is not enough to effect the reconstructions and hence the measurements in any meaningful way. The trend in relative error is of a similar nature however the errors are an order of magnitude smaller than in the method used initially.

Any trend in the measurement variation is less clear to see. However if we ignore the data point at a magnification of 1.5 for S0D1 it could be the case that the variation is decreasing with magnification for a non-ideal detector and vice-versa for a non-ideal source. In order to test this hypothesis a further twenty reconstructions were conducted at magnifications of 1.5, 2.0556 and 4.0; the increase in sample size at these points should give a clearer picture of the underlying measurement variation. It would have been of great interest to conduct more reconstructions at all magnifications but this would have taken far too long - the new samples were chosen to cover low, medium and high magnifications in the hope that any trend became clearer. Figure 7 shows the measurement variation for the higher sampled magnifications. This seems to show that as magnification increases the measurement variability increase for the S1D0

## RESULTS



Figure 6: Showing the variation of the radius measurement at each magnification.

treatment and decreases for the the *S0D1* treatment. In order to further reinforce this conclusion two one tail T-tests where performed to see if the differences in the measurement variation was statistically significant. In the first test, which compares the measurement variance between *S1D0* and *S0D1* at a magnification of 1.5, the null and alternative hypothesis's are given by;

$$H_0 : \sigma_{S1D0,1.5} = \sigma_{S0D1,1.5}$$

$$H_1 : \sigma_{S1D0,1.5} < \sigma_{S0D1,1.5}$$

The test resulted in a test statistic of  $F = 0.1781$  and p-value of  $6.431e - 06 < 0.01$  ( $m=29, n=29$  degrees of freedom), so the null hypothesis can be rejected at the 95% level suggesting that there is significant evidence that  $\sigma_{S1D0,1.5} < \sigma_{S0D1,1.5}$ . For the second test we will compare the measurement variance between *S1D0* and *S0D1* at a magnification of 4.0. The null and alternative hypothesis's are given by;

$$H_0 : \sigma_{S1D0,4.0} = \sigma_{S0D1,4.0}$$

$$H_1 : \sigma_{S1D0,4.0} > \sigma_{S0D1,4.0}$$

The test resulted in a test statistic  $F = 0.1619$  and a p-value of  $2.347e - 06 < 0.01$  ( $m=29, n=29$  degrees of freedom), so the null hypothesis can be rejected at the 95% level suggesting that there is significant evidence that  $\sigma_{S1D0,4.0} > \sigma_{S0D1,4.0}$ .



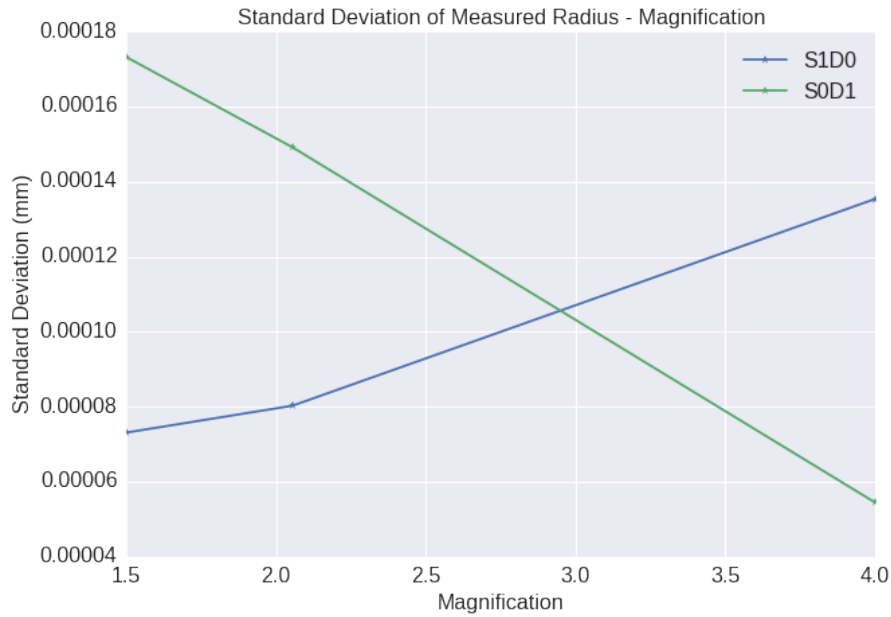


Figure 7: Showing the variation of the radius measurement with a sample of 30 at each magnification.

The result of the two F-tests reinforces the hypothesis that there exists contrasting trends in measurement uncertainty between *S0D1* and *S1D0*. It seems clear that an increase in magnification leads to a decrease in measurement variability for *S0D1* and an increase in the variability for *S1D0* - with an intersection point (position of equal variability) at a magnification of between 2.5 and 3.0. The level of variability in the measurement also relates to the relative error in the measurement; high variability leads to a larger relative error. This can be clearly seen in the error and variability trends of the two treatments *S0D1* and *S1D0*.

Further to the measurements of the radii, the position of the spheres centers were also calculated. Again all measurements resulted in a systematic bias; figure 8 shows the average position for a range of magnifications.

The average position of the centre does not exhibit any clear trend with respect to magnification. There does however seem to be differences between the individual treatments. Both *S0D0* and *S0D1* show little variation in the measured position as magnification varies, whereas *S1D1* and *S1D0* exhibit much greater fluctuations in the measured position. The standard deviation of the measured position, taken over ten repetitions at each magnification, is shown in figure 9. The logarithmic plot shows that the variation is an order of magnitude larger for *S1D0* and *S1D1* than for *S0D1*. This contrasts with the variation in the measured radius for which the standard deviation was approximately of the same magnitude for both *S1D0* and *S0D1*.

## RESULTS

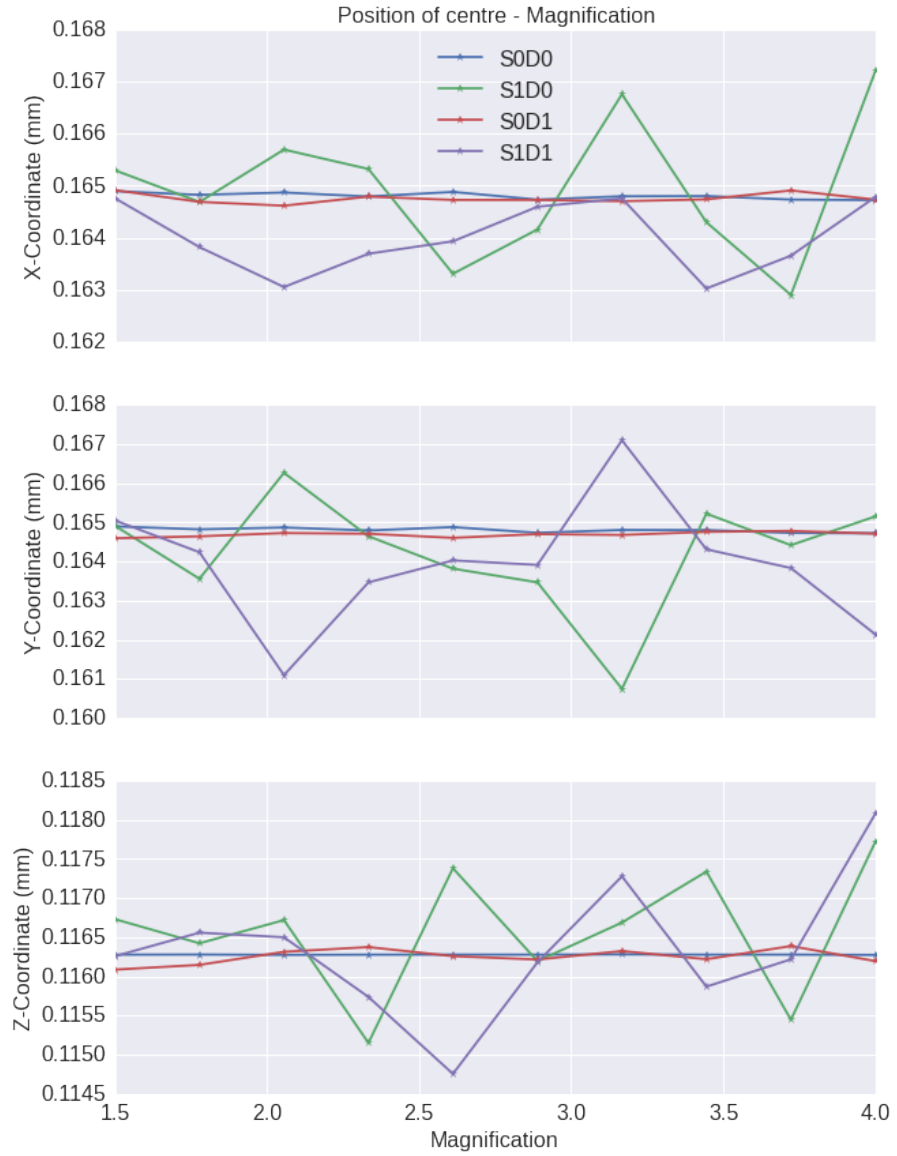


Figure 8: Showing the measured position of the spheres centre

### 4.3 POLYCHROMATIC PROJECTIONS

### 4.4 IMAGE RESOLUTION - MTF HALF WIDTH

The calculation of the MTF half width was obtained from ten repetitions in each of the four treatments (SoDo, S1Do, SoD1 and S1D1) at the same set of magnifications as used in the analysis of the radius. The MTF analysis was performed on the same voxel data as was used previously. Two methods were used in order to obtain the MTF's half width - an approach based on radial rebinning of voxels on coordinate slices (polar method) and one based on the 3D interpolation of voxel data along radial lines (interpolation method).

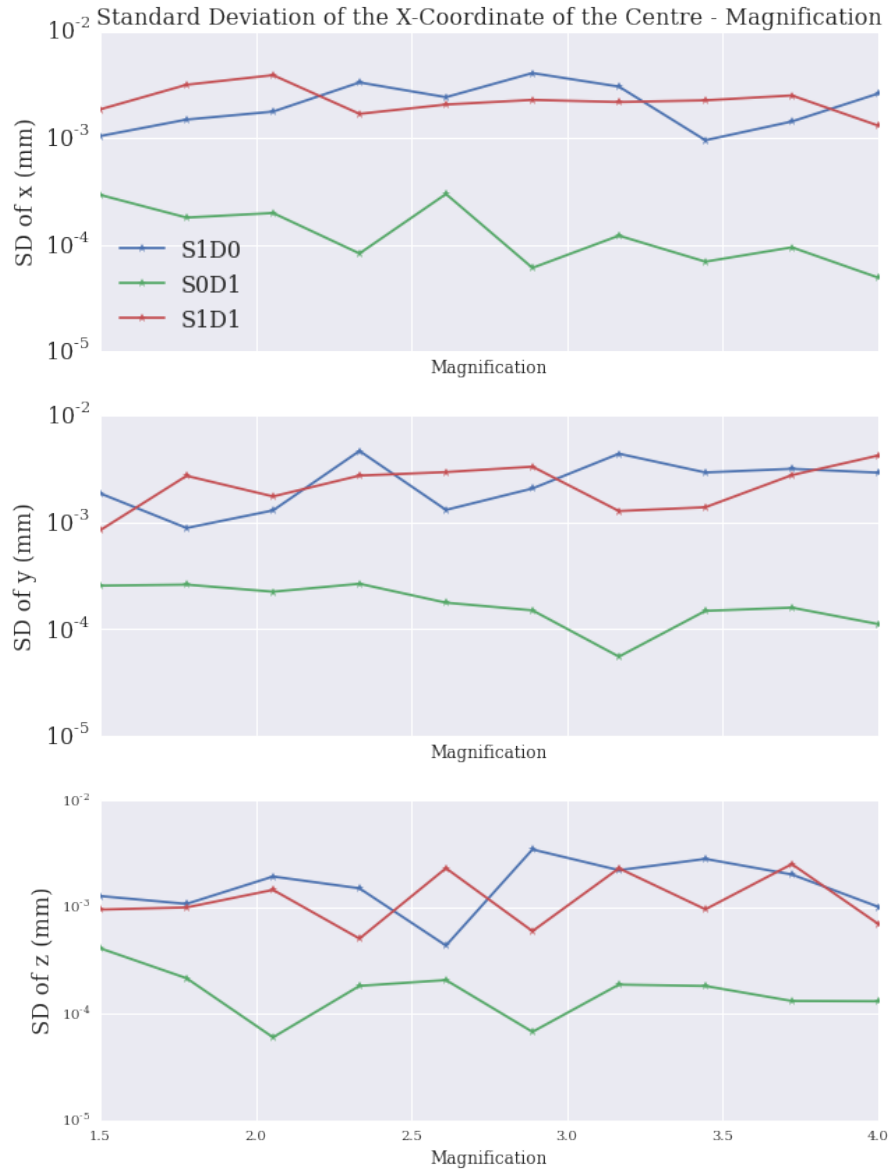


Figure 9: Showing the standard deviation of the measured position of the spheres centre

Each method was applied to data taken from the three coordinate planes (yz-plane, xz-plane and the xy-plane). As can be seen in figure 10 and figure 11 the two methods show a close agreement in the general trends seen - treatment S0D0 is not shown since it has much larger half width values and so the other trends are less visible. Although it was expected that there would be some variation in the measurement using data taken from different planes, due to the non-exact nature of the FDK reconstruction method, this does not seem to be the case in any significant way. The various trends can be seen more clearly in figures 12, 13, 14 and 15.

## RESULTS

Interpolation method - MTF halfwidth as magnification increases

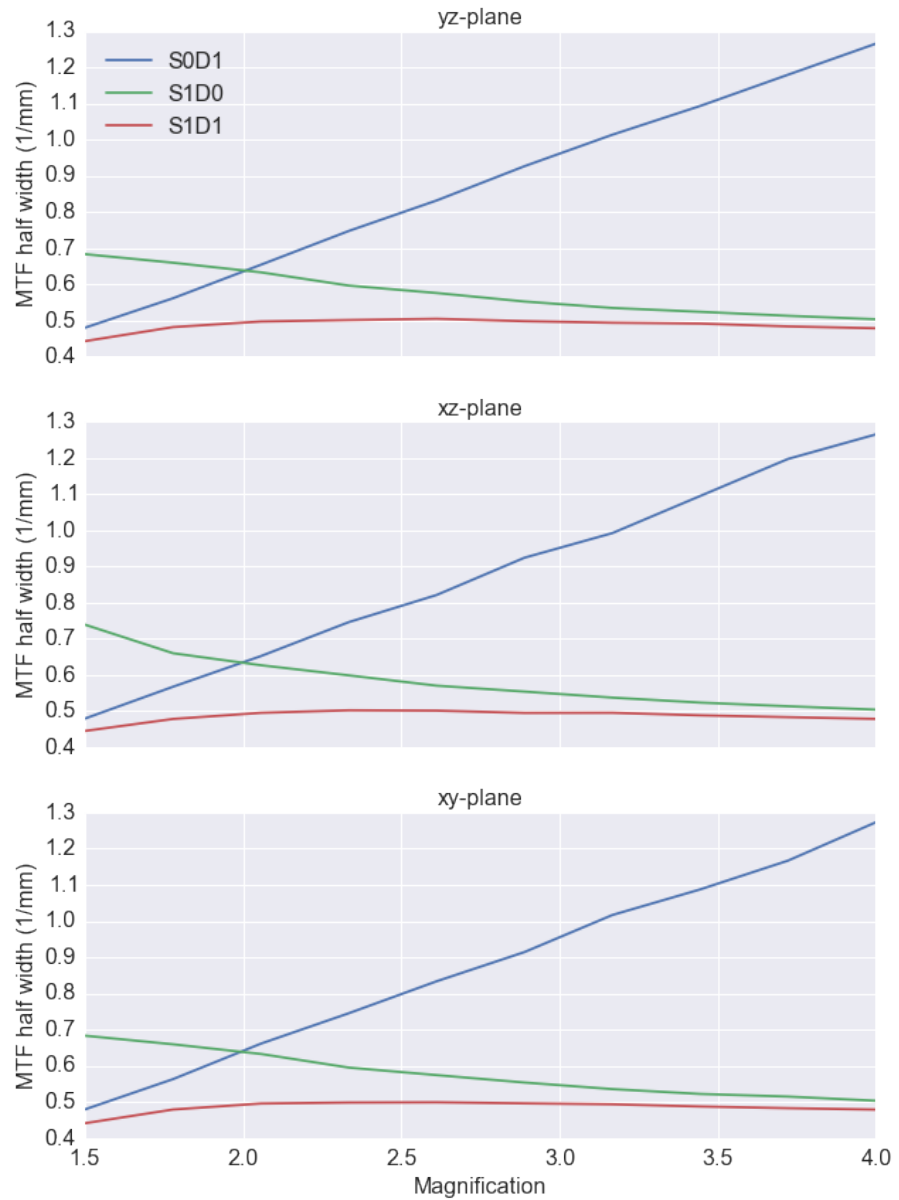


Figure 10: Showing the standard deviation of the measured position of the spheres centre

The S0D0 treatment, shown in figure 12, exhibits a linearly increasing trend but again as in the radius measurements also shows a tendency to be rather noisy. The half width measurements in the yz-plane obtained via the polar method and the measurements in the xz-plane obtained via the interpolation method (shown in howstrange) follow an almost exactly equal trend for all magnifications. The two series agree almost exactly at all points - having checked repeatedly for any errors in the data analysis a reason for this is unknown.

Polar method - MTF halfwidth as magnification increases

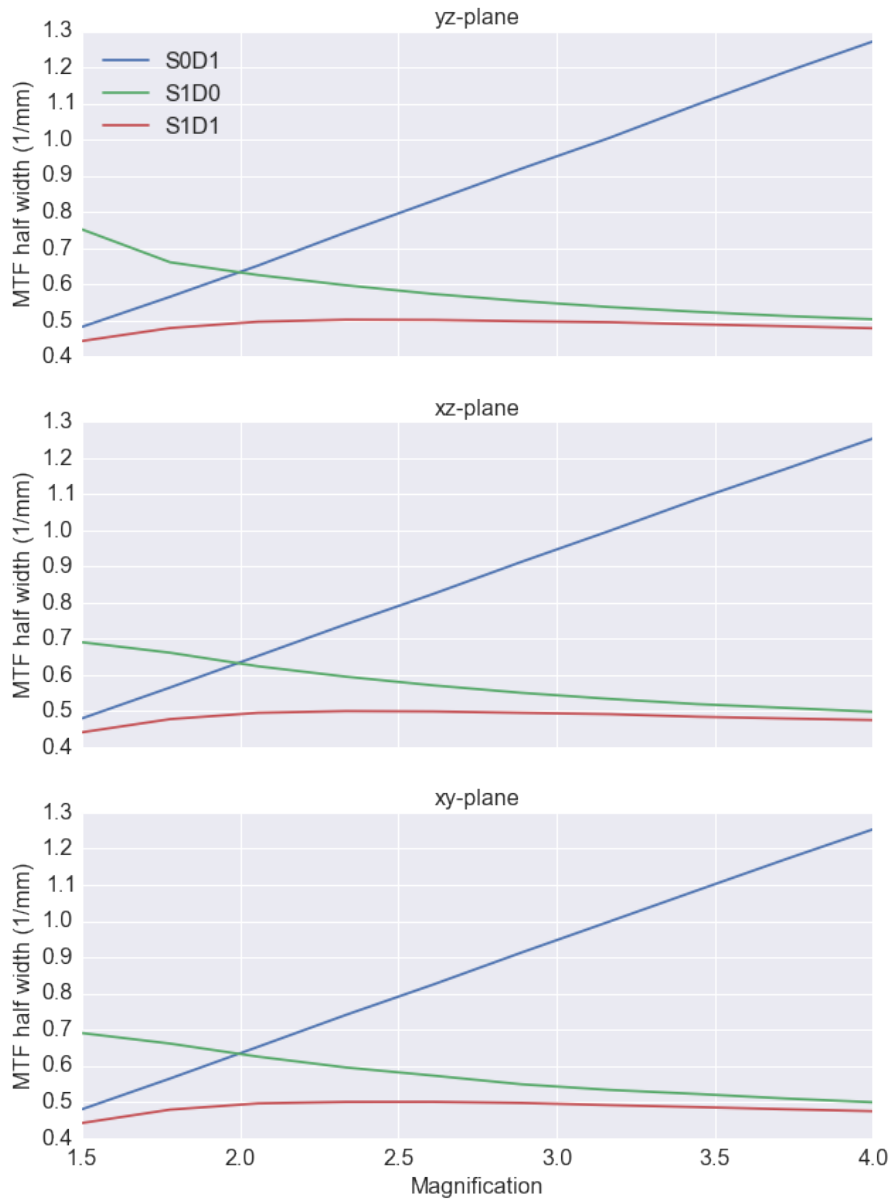


Figure 11: Showing the standard deviation of the measured position of the spheres centre

For the S1D0 treatment (shown in figure 13) the half width measurements show a trend which behaves like an exponential decay curve. The following functional form was fitted to the data;

$$f(x) = A e^{-Bx} + C.$$

The resulting parameters are shown in table 2, along with the RMSE of the fitted model.

## RESULTS



Figure 12: Showing the standard deviation of the measured position of the spheres centre

Table 2:

Method and plane	A	B	C	RMSE
Polar, yz-plane	1.27086332	1.08678843	0.49305544	0.007
Polar, xz-plane	0.61132934	0.57503022	0.43620568	0.002
Polar, xy-plane	0.6119399	0.58143897	0.43846334	0.002
Interp, yz-plane	0.56147878	0.50306134	0.42517996	0.004
Interp, xz-plane	1.07020621	0.98627921	0.48786935	0.005
Interp, xy-plane	0.5631341	0.51761579	0.42994612	0.004

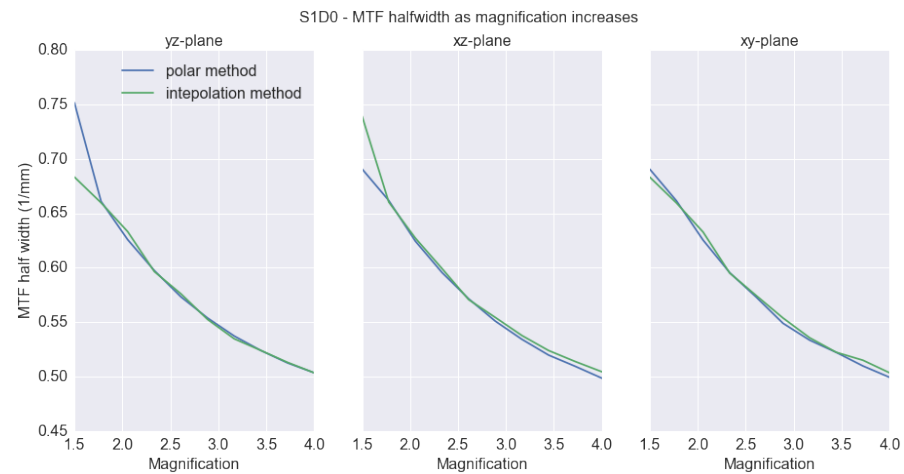


Figure 13: Showing the standard deviation of the measured position of the spheres centre

The S0D1 treatment shows a clear linearly increasing trend in the half widths as magnification increases - this can be seen in figure 14. Again a linear function of the following form was fitted to the data;

Table 3:

Method and plane	A	B	RMSE
Polar, yz-plane	0.31720477	0.002951	0.002
Polar, xz-plane	0.31003435	0.01573987	0.001
Polar, xy-plane	0.31029769	0.01497927	0.001
Interp, yz-plane	0.31577521	0.00678286	0.004
Interp, xz-plane	0.31692495	0.0025919	0.008
Interp, xy-plane	0.31401344	0.01062478	0.007

$$f(x) = Ax + B$$

The fitted parameters of the model are shown in table 3.

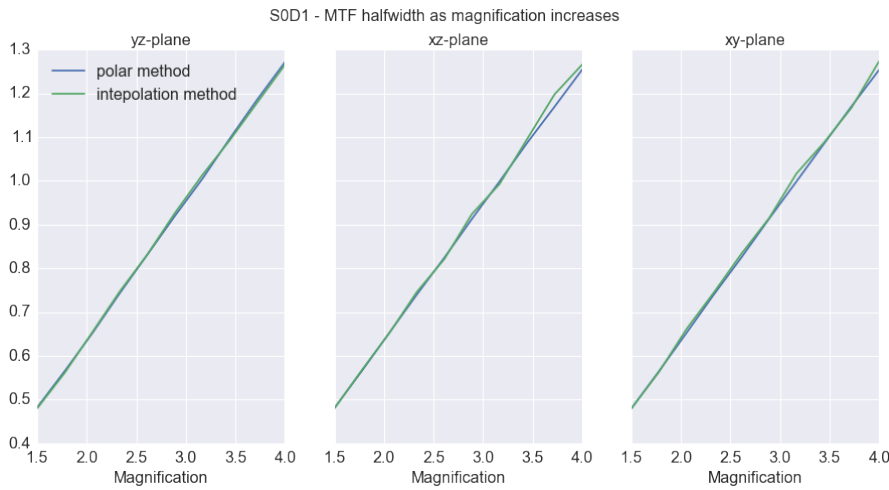


Figure 14: Showing the standard deviation of the measured position of the spheres centre

In the S1D1 treatment, in which offsets are applied to both the source and detector positions, the trend in half width is clearly non-linear - this can be seen in figure 15. In order to test if this trend is a simple linear combination of the two fitted functions for S1D0 and SOD1 the following model was fitted to the data;

$$g(x) = A e^{-Bx} + Cx + D$$

The resulting model parameters are shown in table 4.

## RESULTS

Table 4:

Method and plane	A	B	C	D	RMSE
Polar, yz-plane	-3.01767128	2.35156778	-0.02125605	0.56372268	0.0005
Polar, xz-plane	-3.70124999	2.50146776	-0.02145405	0.56063008	0.0007
Polar, xy-plane	-3.35156301	2.41166283	-0.02300553	0.56631523	0.0004
Interp, yz-plane	-3.71780806	2.49623461	-0.02091193	0.56238338	0.001
Interp, xz-plane	-2.68587678	2.29689752	-0.02093834	0.56232039	0.001
Interp, xy-plane	-4.80161526	2.72103386	-0.0174492	0.54856493	0.0006



Figure 15: Showing the standard deviation of the measured position of the spheres centre



# 5

---

## CONCLUSION

---